Hindawi
International Journal of RF and Microwave Computer-Aided Engineering
Volume 2024, Article ID 8835630, 15 pages
https://doi.org/10.1155/2024/8835630

WILEY | Hindawi

Research Article

Wideband 4×4 Nolen Matrix with 360° Continuously Tuned Differential Phase and Low In-Band Phase Deviation Error

Da Yu, Hongmei Liu, Yan Zhang, Zhongbao Wang, and Shaojun Fang

School of Information Science and Technology, Dalian Maritime University, Dalian, Liaoning 116026, China

Correspondence should be addressed to Hongmei Liu; lhm323@dlmu.edu.cn

Received 6 July 2023; Revised 13 January 2024; Accepted 16 January 2024; Published 27 January 2024

Academic Editor: Phillippe Ferrari

In the paper, a wideband tunable 4×4 Nolen matrix is proposed. By using the presented topology of the Nolen matrix, tunable output port phase differences can be realized by inserting one type of tunable phase shifters (T-PS). Besides, the in-band phase deviation error is minimized by adding compensation phase shifters (C-PSs) to the output ports of the Nolen matrix. Analytical design methods based on signal flow graphs and complex exponential signal are given to obtain the rigorous relationships of the coupling and phase shifts in the Nolen matrix. Besides, a detailed method for output ports phase slope compensation is provided. For validation, a prototype centered at 5.8 GHz is designed and fabricated. Measurement results agree well with the simulated ones. By using only one voltage to control the phase shifts of the T-PS in a 90° range for each input excitation of the Nolen matrix, a full 360° range of the progressive phase difference is realized by switching four input ports. The measured fractional bandwidth under 10 dB return loss and isolation is larger than 24.5% with the in – band ± 1.5 dB amplitude imbalance and ±15° phase deviation error for ports 1-4 excitations. Besides, for a more strict criterion of ±1 dB amplitude imbalance and 10° phase deviation error, the measured bandwidths are larger than 15% for all port excitations.

1. Introduction

With the development of fifth-generation (5G) communication systems, multibeam smart antennas have been a research hotpot, where the essential part is the beamforming network (BFN). Among the reported BFNs, the circuit-based BFNs such as Butler [1], Blass [2], and Nolen matrices [3] are preferred. The more widely used BFN is the Butler matrix, which has the advantages of simple structure, low cost, and convenient design procedure. However, since crossover circuits are essential part in the Butler matrices and the design complexity are increased along with increased ports, various studies have been concentrated on alleviating the complexity [4, 5]. Besides, the Butler matrix usually has 2^N numbers of input/output ports. To achieve arbitrary numbers of output ports, the Blass and Nolen matrices are good candidates. Whereas, due to the use of loads, the efficiency of the Blass matrix is low. As a modification, the Nolen matrix is proposed with theoretically lossless and reduced size.

In the past decades, most of the Butler and Nolen matrices show narrow bandwidths, which is unfit for 5G applications. Although the BFNs in [6–15] exhibit enough bandwidth of impedance matching, the bandwidths for 1 dB output port amplitude imbalance and 10° output port phase differences (PDs) are limited (<5%). It is noted that the evaluation of wideband application should be the overlapped bandwidth, which generally includes 10 dB impedance matching, 10 dB isolation, 1 dB output port amplitude imbalance, and 10° output port phase differences. Thus, many efforts have been done on the overlapped bandwidth improvement of BFNs. The most common method is the phase compensation technique. In [16], the phase correction networks consisted by a number of coupled-line sections are proposed for obtaining wideband phase characteristics of a 4×4 Butler matrix. In [17], a wide bandpass filter is served as the phase compensator in designing the 3×4 Butler matrix, and a wide overlapped bandwidth of more than 60% is achieved. In [18], a 4×4 Nolen matrix with overlapped bandwidth of 40% is presented by using the differential phase shifters to compensate for the phase difference slope between the output ports. Except of the phase compensation technique, the method of removing the components which will deteriorate the output port phase flatness is also effective. In [19], a hybrid coupler with arbitrary phase difference is proposed and applied in the design of a 4×4 Butler matrix. As a result, a wide overlapped bandwidth of 45.3% is obtained by removing the phase shifters and crossovers. Similarly, the phase shifters in a 3×3 Nolen matrix can be ignored by using the wideband hybrid coupler, and a wide overlapped bandwidth of more than 40% is achieved with reduced size [20].

However, the wideband BFNs introduced above can only achieve several fixed beams, which limits the coverage of the multibeam antenna array. To increase the spatial coverage, wideband BFNs with flexible beam controllability are needed. In [21], a 4×4 Butler matrix with equal/unequal phase differences is designed in an overlapped bandwidth of 40% by using an arbitrary phase wideband coupler and several wideband phase shifters. In [22], the progressive phase shifts are obtained in an overlapped bandwidth of 8.3% by cascading extra phase reconfigurable transmission lines to the output ports of a standard Butler matrix. Although the beam controllability is improved in [21, 22], the continuous control of multibeam cannot be realized due to the discrete PDs. Recently, several BFNs with continuously tunable differential phases are presented and regarded as an effective solution to expand the beam controllability. In [23], a tunable 3×3 Nolen matrix is designed by connecting tunable phase shifters (T-PSs) to the outports of the standard Nolen matrix. Under the criterion of $\pm 10^\circ$ PD error, the bandwidth is 3.7%. By integrating two types of T-PSs within the 4×4 Butler matrix, a continuously tuned phase in the range of 360° is realized [24]. However, although the 10 dB impedance bandwidth reaches 15%, the bandwidth for $\pm 10^\circ$ PD error is less than 1%, which is unable to meet the requirements for wideband applications. In [25], four phase shifters are integrated in a modified 2×4 Butler matrix to accomplish the output port phase tunability. The drawback is also the narrow bandwidth for the phase performance. Although several researches have been done on the phase tunable couplers [26–28], which can be used for realizing BFNs with tuned phases, the features of narrow phase tuning range [26, 27] and large in-band phase deviation error [28] limit the realization of wideband phase tuned BFNs. In the authors' previous work, a wideband 2×4 Nolen matrix with a 360° continuously tuned differential phase is presented [29]. However, since two types of the T-PSs have to be used, the insertion loss is still hard to reduce.

In this paper, for the first time, a continuously tuned wideband 4×4 Nolen matrix based on only one type of T-PS is presented. Compared with the other feeding networks, the proposed design has the merits of the following: (1) Only one type of T-PS is integrated inside the Nolen matrix, and a full 360° progressive phase difference is achieved with a compact structure by using one voltage in control; (2) the widest bandwidth with the flattest amplitude and phase progressions among the tunable matrices in existence is exhibited by the proposed continuously tuned Nolen matrix; (3) the T-PS with a 90° phase shift range is enough for obtaining a full 360° differential phase; (4) low in-band phase deviation error and low insertion loss.

2. Theoretical Analysis

Conventionally, the phase shifters in the 4×4 Nolen matrix are irregularly distributed at the through and coupled ports of the coupler [18], which results in circuit complexity and limits the design flexibility. As an improvement, Figure 1 shows the schematic of the proposed 4×4 Nolen Matrix with ports 1-4 as input ports and ports 5-8 as output ports. Each unit in the Nolen matrix is composed of one coupler and one phase shifter connected to the coupled port of the coupler. The coupling of each coupler is defined as C_i, and the phase of the phase shifter is named as φ_i, where $i = 1, 2, 3, \cdots 6$.

In general, the coupler can be characterized by its S-parameters [30], as shown in (1). Here, a_i represents the coupling factor of the coupler. The relationship between the coupling C_i and a_i is $C_i = -20 \text{ lg } (\cos a_i)$. The phases of the through and coupled ports are defined as α_i and β_i, respectively. For a quadrature coupler, the PD between α_i and β_i is $\pm 90^\circ$.

$$[S_c] = \begin{bmatrix} 0 & \sin a_i e^{-j\alpha_i} & \cos a_i e^{-j\beta_i} & 0 \\ \sin a_i e^{-j\alpha_i} & 0 & 0 & \cos a_i e^{-j\beta_i} \\ \cos a_i e^{-j\beta_i} & 0 & 0 & \sin a_i e^{-j\alpha_i} \\ 0 & \cos a_i e^{-j\beta_i} & \sin a_i e^{-j\alpha_i} & 0 \end{bmatrix}. \quad (1)$$

In the following, the theory of the proposed 4×4 Nolen matrix is analyzed. Here, the relationships of the circuit parameters are derived by exciting the input ports individually.

2.1. Input at Port 1. When port 1 is excited, the output port distributions (S_{51} to S_{81}) can be expressed as (2a)–(2d) according to (1).

$$S_{51} = \sin a_1 e^{-j\alpha_1}, \quad (2a)$$

$$S_{61} = \cos a_1 \sin a_2 e^{-j(\phi_1+\beta_1+\alpha_2)}, \quad (2b)$$

$$S_{71} = \cos a_1 \cos a_2 \sin a_3 e^{-j(\phi_1+\phi_2+\beta_1+\beta_2+\alpha_3)}, \quad (2c)$$

$$S_{81} = \cos a_1 \cos a_2 \cos a_3 e^{-j(\phi_1+\phi_2+\beta_1+\beta_2+\beta_3+\phi_3)}. \quad (2d)$$

Since the output port amplitudes (AP) and PDs should be equal for a general Nolen matrix, the relationships in (3a) and (3b) can be derived using (2a)–(2d) when C_2 and

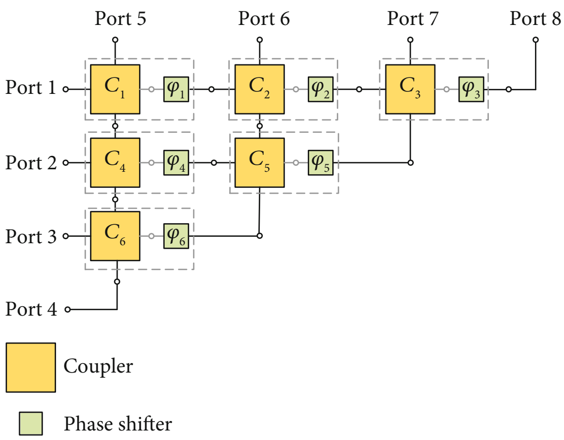

Figure 1: The preliminary schematics of the proposed 4×4 Nolen matrix.

C_3 use the same type of coupler ($\alpha_2 = \alpha_3$). Besides, the PD for port 1 excitation ($\Delta\varphi_1$) can be expressed as (3c).

$$\cos a_1 = \frac{\sqrt{3}}{2}, \quad \cos a_2 = \frac{\sqrt{2}}{\sqrt{3}}, \quad \cos a_3 = \frac{1}{\sqrt{2}}, \tag{3a}$$

$$\phi_1 = \phi_2, \quad \phi_3 = \phi_1 + \alpha_2, \tag{3b}$$

$$\Delta\phi_1 = -\beta_2 - \phi_1. \tag{3c}$$

2.2. Input at Port 2. When port 2 is the input port, the signal passes through multiple paths to reach the output port. Thus, the transmission parameters under port 2 excitation can be expressed by the superposition of the transmission parameters under multiple paths, as shown in.

$$S_{52} = \sin a_4 \cos a_1 e^{-j(\beta_1+\alpha_4)}, \tag{4a}$$

$$S_{62} = \sin a_4 \sin a_1 \sin a_2 e^{-j(\varphi_1+\alpha_1+\alpha_2+\alpha_4)} + \cos a_4 \sin a_5 \cos a_2 e^{-j(\varphi_4+\alpha_5+\beta_2+\beta_4)}, \tag{4b}$$

$$S_{72} = \sin a_4 \cos a_2 \sin a_1 \sin a_3 e^{-j(\varphi_1+\varphi_2+\alpha_1+\alpha_3+\alpha_4+\beta_2)} + \cos a_4 \sin a_5 \sin a_2 \sin a_3 e^{-j(\varphi_2+\varphi_4+\alpha_2+\alpha_3+\alpha_5+\beta_4)} + \cos a_4 \cos a_5 \cos a_3 e^{-j(\varphi_5+\varphi_4+\beta_3+\beta_4+\beta_5)}, \tag{4c}$$

$$S_{82} = \sin a_4 \cos a_2 \sin a_1 \cos a_3 e^{-j(\varphi_1+\varphi_2+\varphi_3+\alpha_1+\alpha_4+\beta_2+\beta_3)} + \cos a_4 \sin a_5 \sin a_2 \cos a_3 e^{-j(\varphi_2+\varphi_4+\varphi_3+\alpha_2+\alpha_5+\beta_4+\beta_3)} + \cos a_4 \cos a_5 \sin a_3 e^{-j(\varphi_5+\varphi_4+\varphi_3+\alpha_3+\beta_4+\beta_5)}. \tag{4d}$$

Since the designed 4×4 Nolen matrix has equal outputs under different input port excitations, the AP of each output ports is 1/2. After setting $|S_{52}| = 1/2$, the value of $\sin a_4$ is calculated as $1/\sqrt{3}$ according to (4a). Similarly, when the AP of S_{62} is 1/2, the value of $\sin a_5$ is calculated as 1/2 under the condition that the two terms in (4b) have the same exponents. If C_4 and C_2 use the same coupler ($\alpha_4 = \alpha_2$), C_5 and C_1 use the same coupler ($\alpha_5 = \alpha_1$), the relationship between φ_4 and φ_1 can be derived, as shown in.

$$\varphi_4 = \varphi_1 + 2(\alpha_2 - \beta_2). \tag{5}$$

Then, substitute (3b) and (5) into (4a)–(4d), the transmission parameters under port 2 excitation can be reduced to

$$S_{52} = \frac{1}{2} e^{-j(\beta_1+\alpha_4)}, \quad S_{62} = \frac{1}{2} e^{-j(\varphi_1+\alpha_1+\alpha_2+\alpha_4)}, \quad S_{72} = \frac{1}{2} e^{-j(\varphi_1+\varphi_5+\alpha_2\times 2+\beta_5)}, \quad S_{82} = \frac{1}{2} e^{-j(\varphi_1\times 2+\varphi_5+\alpha_2\times 4-\beta_2+\beta_5)}. \tag{6}$$

Based on (6), the expression of φ_5 can be derived under the condition that the output port PDs are equal, as (7a) shows. And the PD $\Delta\varphi_2$ for port 2 excitation is expressed in (7b)

$$\phi_5 = \phi_1 + \alpha_2 \times 3 - \beta_2 \times 2 \tag{7a}$$

$$\Delta\phi_2 = \beta_2 - \alpha_2 \times 2 - \phi_1 \tag{7b}$$

2.3. Input at Ports 3 and 4. Similarly, the transmission parameters under port 3 excitation are listed in (8a)–(8d). Set $|S_{53}| = 1/2$, the value of $\sin a_6$ is calculated as $1/\sqrt{2}$ according to

$$S_{53} = \sin a_6 \cos a_4 \cos a_1 e^{-j(\alpha_6+\beta_1+\beta_4)}, \tag{8a}$$

$$S_{63} = \sin a_6 \cos a_4 \sin a_1 \sin a_2 e^{-j(\varphi_1+\alpha_1+\alpha_2+\alpha_6+\beta_4)} + \sin a_6 \sin a_4 \sin a_5 \cos a_2 e^{-j(\varphi_4+\alpha_4+\alpha_5+\alpha_6+\beta_2)} + \cos a_6 \cos a_5 \cos a_2 e^{-j(\varphi_6+\beta_2+\beta_5+\beta_6)}, \tag{8b}$$

$$S_{73} = \sin a_6 \cos a_4 \sin a_1 \cos a_2 \sin a_3 e^{-j(\varphi_1+\varphi_2+\alpha_1+\alpha_3+\alpha_6+\beta_2+\beta_4)} + \sin a_6 \sin a_4 \sin a_5 \sin a_2 \sin a_3 e^{-j(\varphi_4+\varphi_2+\alpha_2+\alpha_3+\alpha_4+\alpha_5+\alpha_6)} + \sin a_6 \sin a_4 \cos a_5 \cos a_3 e^{-j(\varphi_4+\varphi_5+\alpha_4+\alpha_6+\beta_3+\beta_5)} + \cos a_6 \cos a_5 \sin a_2 \sin a_3 e^{-j(\varphi_6+\varphi_2+\alpha_2+\alpha_3+\beta_5+\beta_6)} + \cos a_6 \sin a_5 \cos a_3 e^{-j(\varphi_6+\varphi_5+\alpha_5+\beta_3+\beta_6)}, \tag{8c}$$

Table 1: Calculated couplings and phase relations in the Nolen matrix.

Coupling C_i	$C_1 = C_5 = 1.25$ dB, $C_2 = C_4 = 1.76$ dB, $C_3 = C_6 = 3$ dB
PS φ_i	$\varphi_2 = \varphi_1$, $\varphi_3 = \varphi_1 + \alpha_2$, $\varphi_4 = \varphi_1 + 2(\alpha_2 - \beta_2)$, $\varphi_5 = \varphi_1 + 3\alpha_2 - 2\beta_2$, $\varphi_6 = \varphi_1 + 2\alpha_2 - \beta_2$
PD $\Delta\varphi_n$	$\Delta\varphi_1 = -\beta_2 - \varphi_1$, $\Delta\varphi_2 = \beta_2 - 2\alpha_2 - \varphi_1$, $\Delta\varphi_3 = -\alpha_2 - \varphi_1$, $\Delta\varphi_4 = 2\beta_2 - 3\alpha_2 - \varphi_1$

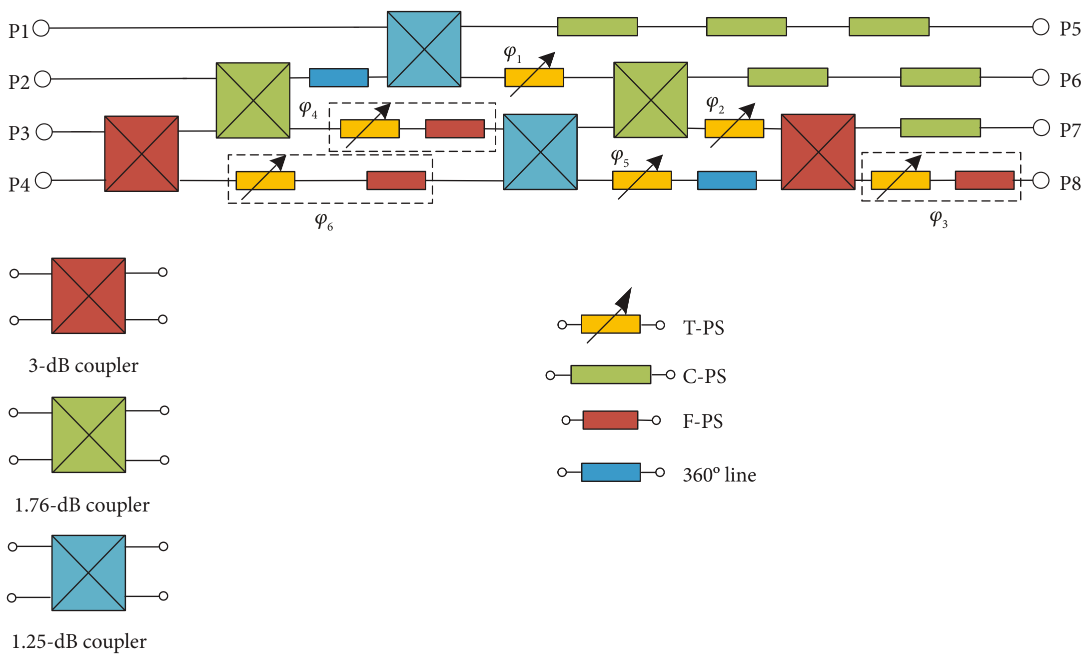

Figure 2: Configuration of the designed 4×4 Nolen matrix.

$$
\begin{aligned}
S_{83} = {} & \sin a_6 \cos a_4 \sin a_1 \cos a_2 \cos a_3 e^{-j(\varphi_1+\varphi_2+\varphi_3+\alpha_1+\alpha_6+\beta_2+\beta_3+\beta_4)} \\
& + \sin a_6 \sin a_4 \sin a_5 \sin a_2 \cos a_3 \mathrm{e}^{-j(\varphi_4+\varphi_2+\varphi_3+\alpha_2+\alpha_4+\alpha_5+\alpha_6+\beta_3)} \\
& + \sin a_6 \sin a_4 \cos a_5 \sin a_3 e^{-j(\varphi_4+\varphi_5+\varphi_3+\alpha_3+\alpha_4+\alpha_6+\beta_5)} \\
& + \cos a_6 \cos a_5 \sin a_2 \cos a_3 e^{-j(\varphi_6+\varphi_2+\varphi_3+\alpha_2+\beta_3+\beta_5+\beta_6)} \\
& + \cos a_6 \sin a_5 \sin a_3 e^{-j(\varphi_6+\varphi_5+\varphi_3+\alpha_3+\alpha_5+\beta_6)}.
\end{aligned}
\tag{8d}
$$

Equations (8a)–(8d) can be reduced to (9) when substituting the relationships in (3b), (5), and (7a) and using the same coupler to realize C_6 and C_3 ($\alpha_6 = \alpha_3$).

$$
\begin{aligned}
S_{53} &= \frac{1}{2} e^{-j(\beta_1+\beta_4+\alpha_6)}, \\
S_{63} &= \frac{1}{2} e^{-j(\varphi_6+\beta_2+\beta_5+\beta_6)}, \\
S_{73} &= \frac{1}{2} e^{-j(\varphi_1+\varphi_2+\alpha_2\times 7-\beta_2\times 3+\beta_5)}, \\
S_{83} &= \frac{1}{2} e^{-j(\varphi_6+\varphi_1\times 2+\alpha_2\times 5+\alpha_5-\beta_2)}.
\end{aligned}
\tag{9}
$$

Using the relation of equal PDs, the expression of φ_6 and the PD $\Delta\varphi_3$ for port 3 excitation are derived and listed in (10a) and (10b), respectively.

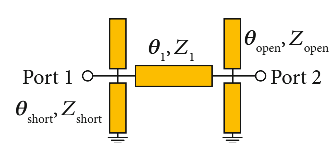

Figure 3: The schematic of the open/shorted-stub-loaded TL.

$$\phi_6 = \phi_1 + \alpha_2 \times 2 - \beta_2, \tag{10a}$$

$$\Delta\phi_3 = -\alpha_2 - \phi_1. \tag{10b}$$

Since the inputs at ports 3 and 4 are both through coupler C_6, the analysis for port 4 excitation is similar with port 3 excitation. Thus, the expressions of the transmission parameters are omitted. Only express the results of the PD $\Delta\varphi_4$ for port 4 excitation.

$$\Delta\phi_4 = \beta_2 \times 2 - \alpha_2 \times 3 - \phi_1. \tag{11}$$

Based on the above analysis, the coupling factor $a_1 - a_6$ can be calculated. Then, the corresponding coupling coefficients $C_1 - C_6$ are obtained. Table 1 shows the calculated coupling coefficients of the couplers in the 4×4 Nolen matrix. The expressions of phase shifters used and the output port PDs are also summarized in Table 1. It is seen from the PDs that when the phase of the through and coupling ports in the coupler C_2 (α_2 and β_2) is fixed, the output port

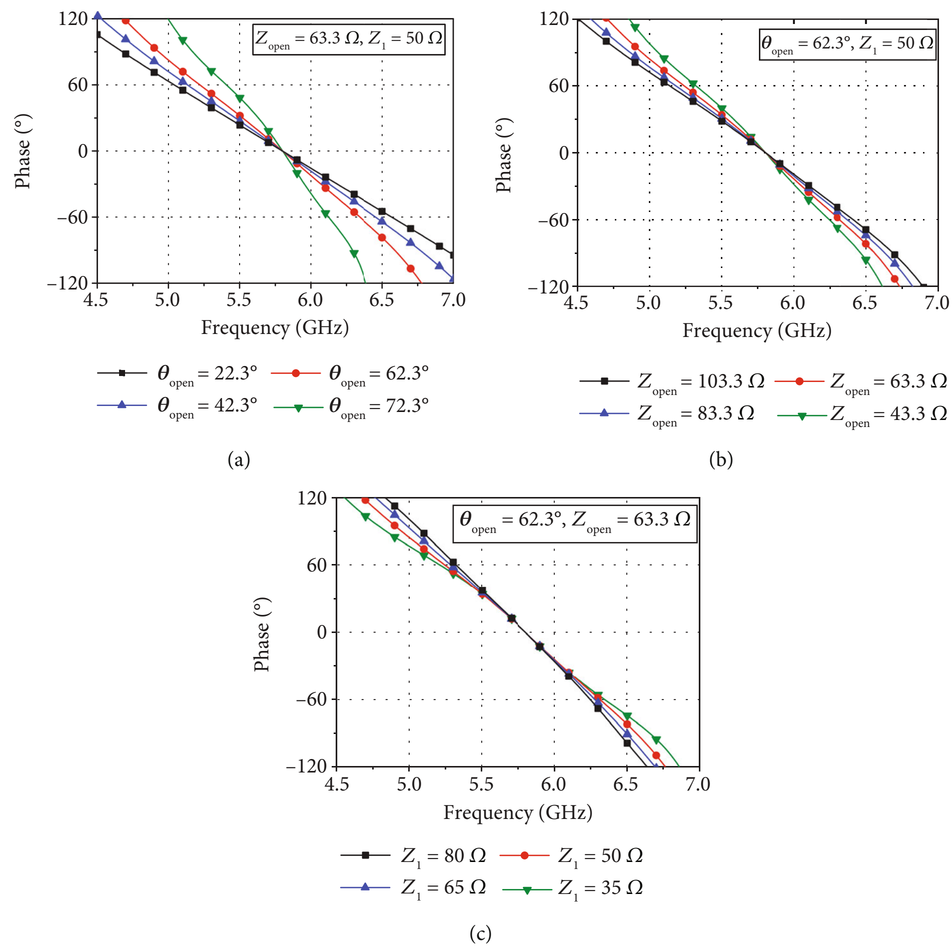

FIGURE 4: Simulated phases of the C-PS3 versus (a) θ_{open}, (b) Z_{open}, and (c) Z_1.

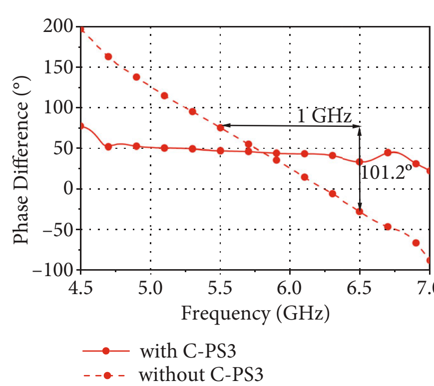

FIGURE 5: Simulated PD between ports 7 and 8 without and with the C-PS3.

TABLE 2: The circuit parameters of different C-PSs and F-PSs.

	θ_{short} (Ω)	θ_{open} (°)	Z_{short} (Z_{open}) (Ω)	θ_1 (°)	Z_1 (Ω)
C-PS1	27.7	62.3	63.6	360	53.9
C-PS2	27.7	62.3	63.6	360	53.9
C-PS3	27.7	62.3	63.6	360	53.9
180° F-PS	44.4	45.6	70.1	180	60.0
90° F-PS	39.6	50.4	83.3	450	63.6

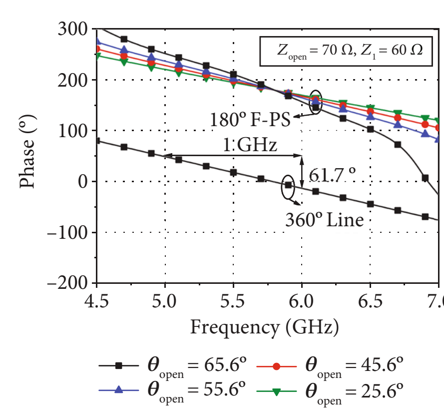

FIGURE 6: Simulated phase of the 180° F-PS and 360° line.

PDs under different input port excitations are varied with φ_1, which indicates that the phase tunability of the Nolen matrix can be performed by changing the value of φ_1.

3. Design and Compensation Method

Figure 2 shows the configuration of the designed 4×4 Nolen matrix. Since the branch-line couplers (BLCs) [31] have the

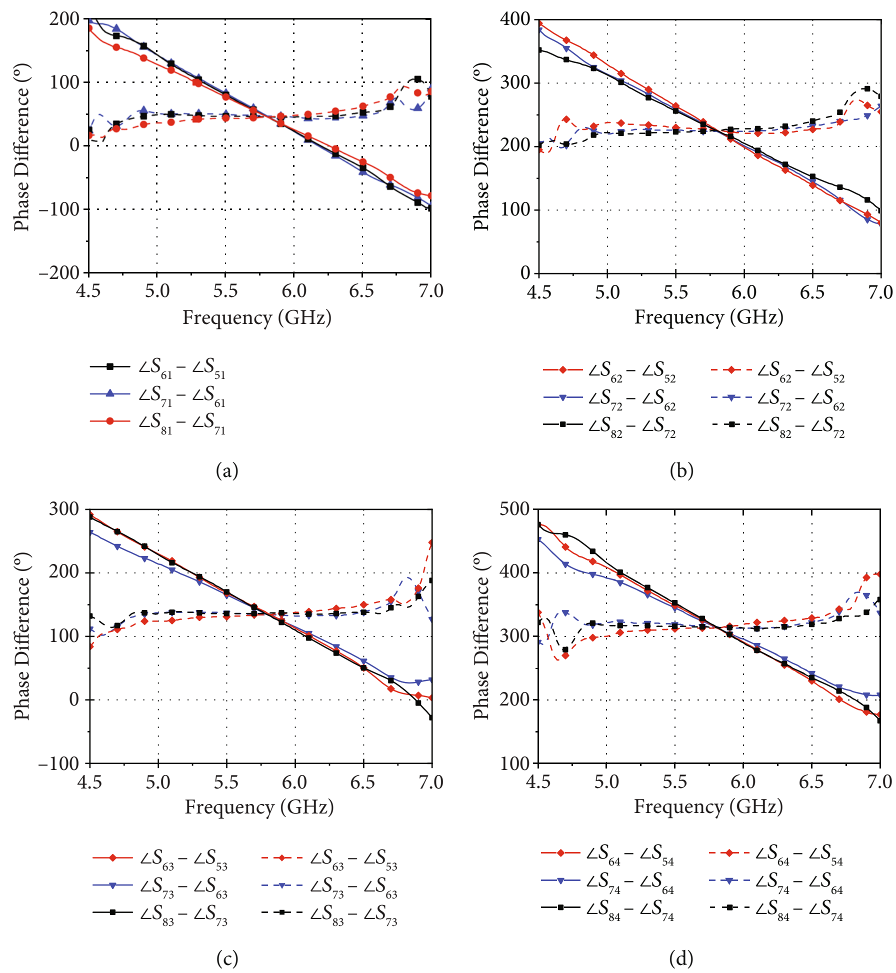

FIGURE 7: The PD comparison before (solid line with symbol) and after (dash line with symbol) compensation. (a) Port 1 excitation. (b) Port 2 excitation. (c) Port 3 excitation. (d) Port 4 excitation.

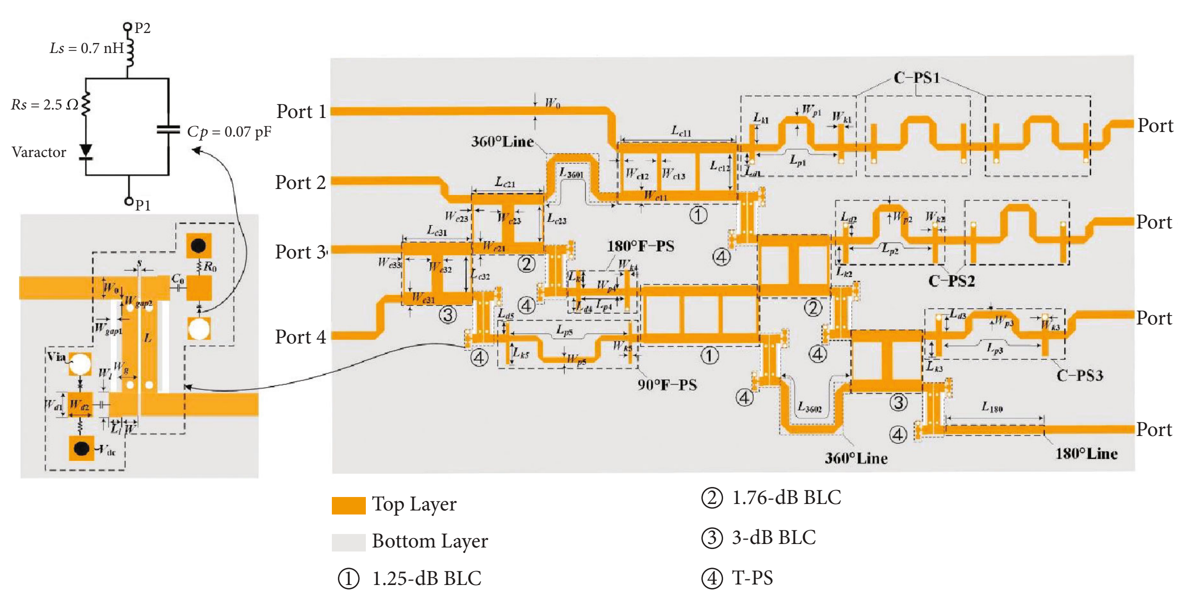

FIGURE 8: Topology of the fabricated wideband 4 × 4 Nolen matrix with tunable differential phase.

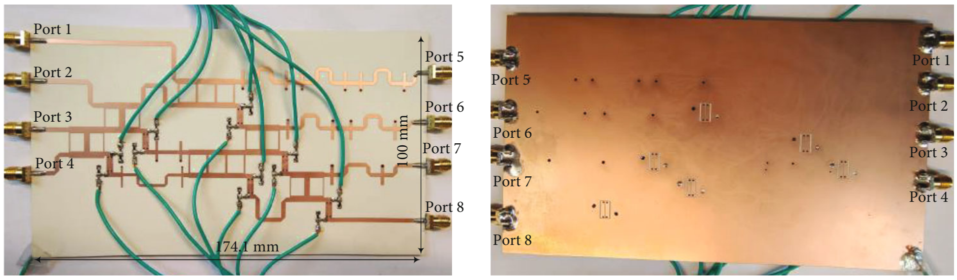

Figure 9: (a) Top and (b) bottom view of the fabricated Nolen matrix.

Table 3: Dimensions of the fabricated Nolen matrix. Unit: mm.

The BLCs	$L_{c11} = 25.0$, $L_{c12} = 8.0$, $W_{c11} = 2.3$, $W_{c12} = 0.9$, $W_{c13} = 0.6$, $L_{c21} = 15.5$, $L_{c22} = 8.1$, $W_{c21} = 2.5$, $W_{c22} = 2.4$, $W_{c23} = 0.6$, $L_{c31} = 15.2$, $L_{c32} = 8.1$, $W_{c31} = 2.7$, $W_{c32} = 2.4$, $W_{c33} = 0.3$
The C-PSs	$L_{p1} = 30.2$, $L_{k1} = 4.3$, $L_{d1} = 2.8$, $W_{p1} = 1.6$, $W_{k1} = 1.2$, $L_{p2} = 32.2$, $L_{k2} = 4.2$, $L_{d2} = 3.1$, $W_{p2} = 1.6$, $W_{k2} = 1.2$, $L_{p3} = 30.6$, $L_{k3} = 3.7$, $L_{d3} = 3.8$, $W_{p3} = 1.6$, $W_{k3} = 1.2$
The F-PSs	$L_{p4} = 12.6$, $L_{k4} = 4.0$, $L_{d4} = 3.5$, $W_{p4} = 1.8$, $W_{k4} = 1.0$, $L_{p5} = 37.7$, $L_{k5} = 5.0$, $L_{d5} = 3.2$, $W_{p5} = 1.2$, $W_{k5} = 0.7$
The T-PS	$W = 1.3$, $L = 11$, $W_g = 1.2$, $s = 0.2$, $W_l = 2$, $L_l = 1$, $W_{d1} = 2$, $W_{d2} = 2$, $W_{\mathrm{gap1}} = 0.3$, $W_{\mathrm{gap2}} = 0.2$, $R_0 = 1\,\mathrm{k}\Omega$, $C_0 = 1\,\mu\mathrm{F}$
Others	$W_0 = 1.8$, $L_{3601} = 32.1$, $L_{3602} = 33.5$, $L_{180} = 14.2$

advantages of simple structure and easy fabrication, they are adopted in realizing the Nolen matrix. Here, two types of BLCs are used, where the three-BLC corresponds to the couplings of 3 dB and 1.76 dB, and the four-BLC is used for realizing the coupling of 1.25 dB. It is noted that for better layout in practical processing, two 360° transmission lines (TLs) are added to the isolated port of coupler C_1 and C_3.

According to Table 1, it is found that when the coupler C_2 is assigned (α_2 and β_2 are known), the phase shifts of the PSs ($\varphi_2 - \varphi_5$) are also expressed by φ_1. When the value of φ_1 is varied for obtaining controllable phases of the Nolen matrix, the phase shifts $\varphi_2 - \varphi_5$ are also changed, which results in too many T-PSs with different phases. To solve the problem and reduce the type of T-PS, the phase shifts $\varphi_2 - \varphi_5$ are replaced by a T-PS and a fix phase shifter (F-PS), where the T-PS has the same phase shifts of φ_1.

In the design, the couplers C_1 and C_5 are realized by four BLCs, and the three BLCs are used for constructing the couplers C_2, C_3, C_4, and C_6. Then, the phases of the through and coupled ports are obtained as follows: $\alpha_1 = \alpha_5 = 270°$, $\beta_1 = \beta_5 = 360°$, $\alpha_2 = \alpha_3 = \alpha_4 = \alpha_6 = 180°$, and $\beta_2 = \beta_3 = \beta_4 = \beta_6 = 270°$. Thus, the φ_i $(i = 1, 2, 3, \cdots 6)$ in (3b), (5), (7a), and (10a) can be simplified as

$$\phi_1 = \phi_2 = \phi_5, \tag{12a}$$

$$\phi_3 = \phi_4 = \phi_1 + 180\circ, \tag{12b}$$

$$\varphi_6 = \varphi_1 + 90\circ. \tag{12c}$$

Based on (12), it is clear that no F-PSs are existed in the phase shifters with phases of φ_2 and φ_5. In the PSs with the phase shifts of φ_3 and φ_4, a 180° F-PS is combined with φ_1 for realization. While a 90° PS is inserted after φ_1 to realize the phase shifts of φ_6. Figure 2 shows the constructions of each phase shifts. By using the replacement method, one type T-PS with phase shifts of φ_1 is enough for realizing the phase tunability of the Nolen matrix.

To obtain full 360° tuned differential phase within the designed wideband Nolen matrix, the T-PS should feature the characteristics of wideband and more than 90° tuned phase shifts. Besides, low loss and stable phase-to-frequency performances are also important for obtaining low in-band amplitude and phase errors. In the design, the T-PS in [26] is adopted for satisfying the above requirements.

Furthermore, to ensure that the PDs between the output ports of the Nolen matrix remain at minimum error in the operation band, the slope of the phase-to-frequency curves of all output ports needs to be consistent. However, since the signal paths are unequal when transferred to the different output ports (ports 5 to 8), the slope of the phase-to-frequency curves at the output ports shows big differences.

Table 4: The output port phase differences corresponding to bias voltages.

Phase difference (°)	Port 1	Port 2	Port 3	Port 4
$V_{\mathrm{dc}} = 20$ V	49	-134	-226	-42
$V_{\mathrm{dc}} = 17$ V	40	-143	-231	-53
$V_{\mathrm{dc}} = 15$ V	33	-148	-238	-60
$V_{\mathrm{dc}} = 13$ V	27	-151	-244	-68
$V_{\mathrm{dc}} = 10$ V	0	-180	-261	-89
$V_{\mathrm{dc}} = 9$ V	-21	-205	-298	-113
$V_{\mathrm{dc}} = 7$ V	-48	-232	-319	-134
$V_{\mathrm{dc}} = 5$ V	-83	-263	-349	-172

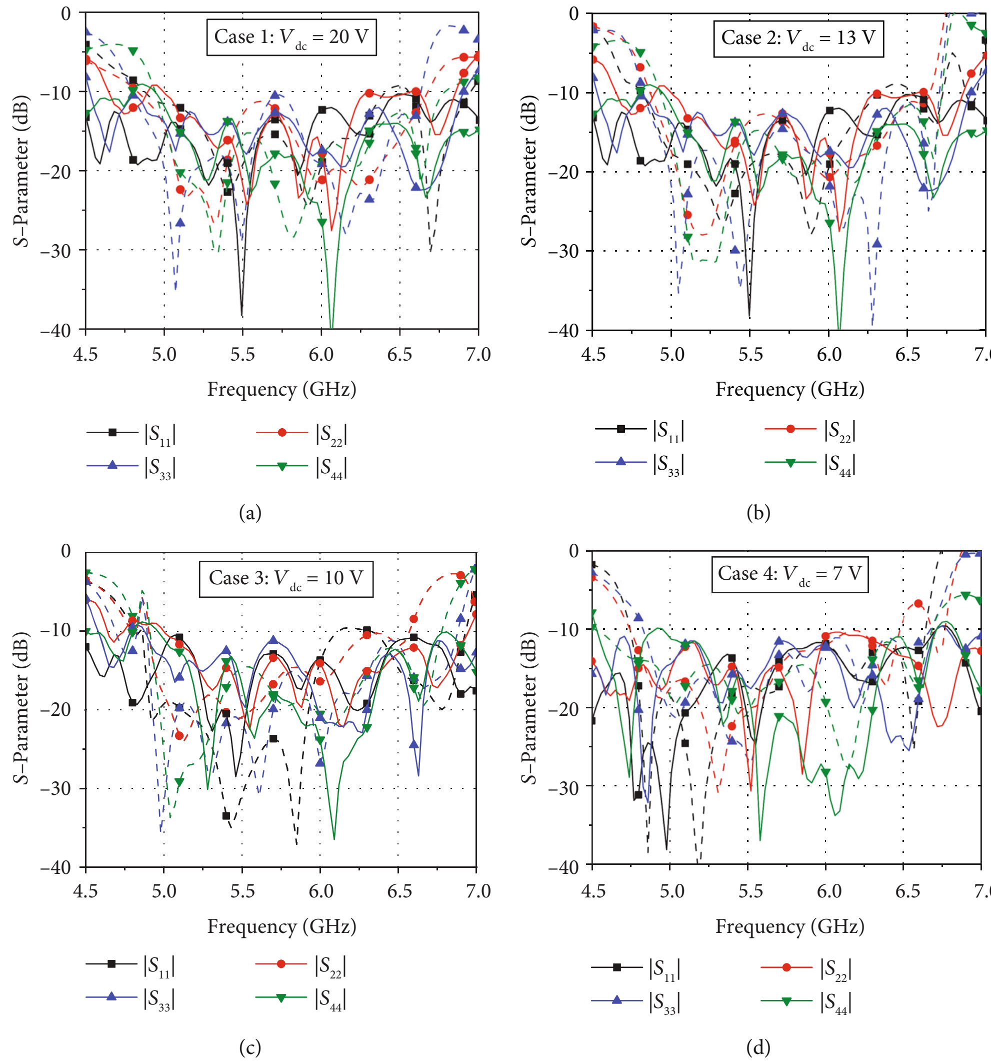

Figure 10: Simulated and measured return loss of the input ports (measured results: solid line with symbol, simulated results: dash line with symbol). (a) Case 1, (b) case 2, (c) case 3, and (d) case 4.

For example, due to the fact that the path of the signal transfers to port 5 is shorter compared with port 8, the slope of the phase-to-frequency curve at port 5 is smaller than that at port 8, which results in large in-band PD error when no compensation technique is applied. To minimize the in-band phase deviation error, the compensation phase shifters (C-PSs) are inserted before the output ports. In detail, one C-PS is inserted to port 7, two C-PSs are inserted to port 6, and three C-PSs are added to port 5. In the following, the compensation processes with PSs are mainly introduced.

3.1. Compensation Process. The C-PS and F-PS (except of the F-PS in φ_3) are both realized by simple open/shorted-stub-loaded TL shown in Figure 3. Since the C-PSs are utilized for phase compensation, the F-PS before port 8 can be implemented using simple TL. Let θ_1 and Z_1 represent the electrical length and impedance characteristic of the TL. The electrical lengths and impedance characteristics of the open/shorted-stub are denoted as $\theta_{open}/\theta_{short}$ and Z_{open}/Z_{short}, separately.

According to Figure 3, the S-parameters of the open/shorted-stub-loaded TL can be expressed, as shown in (13a) and. Here, Z_0 is the port impedance and equals to $50\,\Omega$. Let f_0 and f be the center and operating frequencies, respectively.

$$S_{11\_PS} = \frac{j[(Z_1/Z_0)\sin(\theta_1(f/f_0)) - m_1]}{2[\cos(\theta_1(f/f_0)) - aZ_1\sin(\theta_1(f/f_0))] + j[(Z_1/Z_0)\sin(\theta_1(f/f_0)) + m_1]}, \tag{13a}$$

$$S_{21\_PS} = \frac{2}{2[\cos(\theta_1(f/f_0)) - aZ_1\sin(\theta_1(f/f_0))] + j[(Z_1/Z_0)\sin(\theta_1(f/f_0)) + m_1]}, \tag{13b}$$

where

$$m_1 = 2aZ_0\cos\left(\theta_1\frac{f}{f_0}\right) + \frac{Z_0}{Z_1}\sin\left(\theta_1\frac{f}{f_0}\right) - a^2Z_1Z_0\sin\left(\theta_1\frac{f}{f_0}\right), \tag{14a}$$

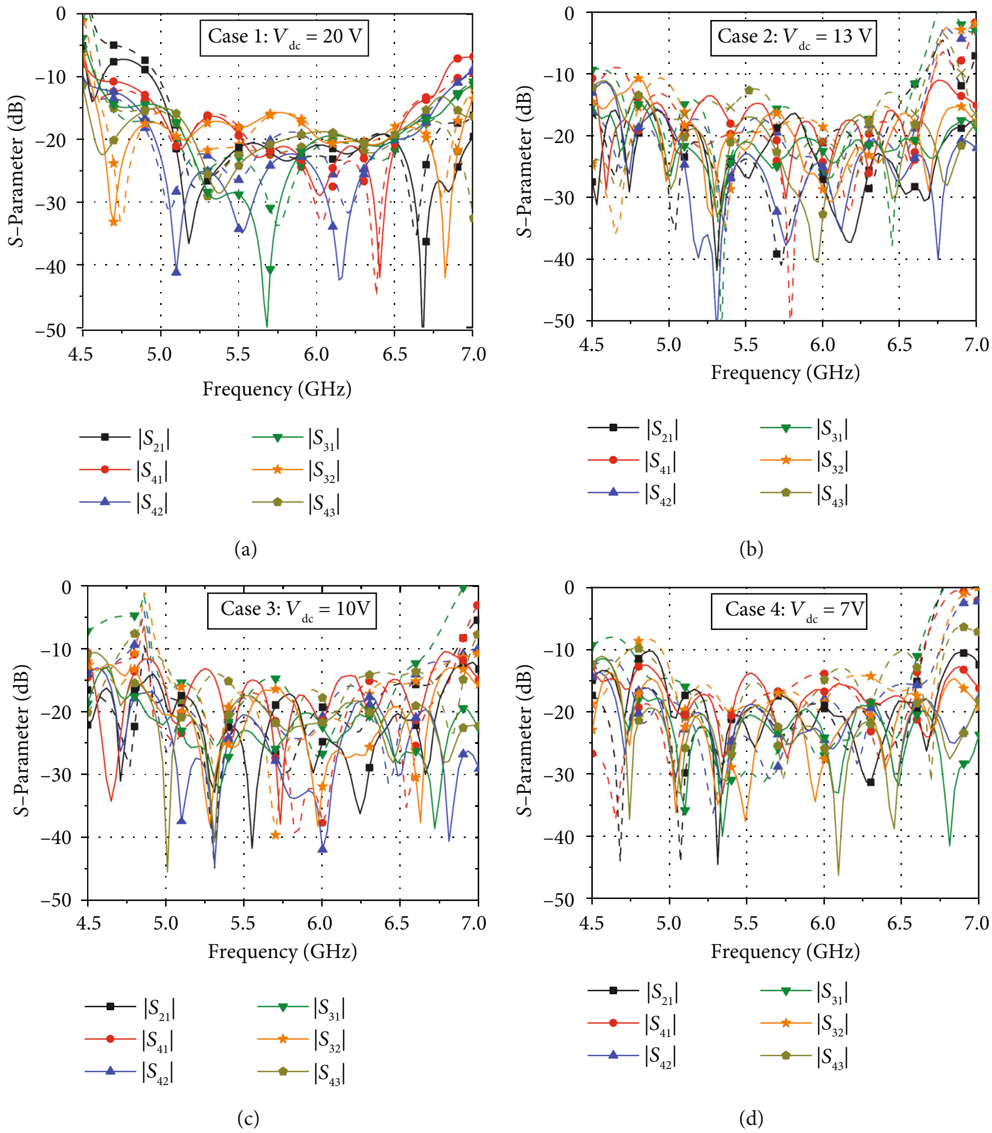

FIGURE 11: Simulated and measured isolation between the input ports (measured results: solid line with symbol, simulated results: dash line with symbol). (a) case 1, (b) case 2, (c) case 3, and (d) case 4.

$$a = \frac{\tan\left(\theta_{open}(f/f_0)\right)}{Z_{open}} - \frac{\cot\left(\theta_{short}(f/f_0)\right)}{Z_{short}}. \tag{14b}$$

According to (13b), the phase shift of open/shorted-stub-loaded TL can be obtained as

$$\theta(f) = -\arctan\frac{[(Z_1/Z_0)\sin(\theta_1(f/f_0)) + m_1]}{2[\cos(\theta_1(f/f_0)) - aZ_1\sin(\theta_1(f/f_0))]}. \tag{15}$$

It can be found from (14b) that the value of a is equal with 0 at the center frequency of f_0 when defining $\theta_{short} + \theta_{open} = 90^\circ$ and $Z_{open} = Z_{short}$. Substitute $a = 0$ into (15) and assign $\theta_1 = n\pi/2$, the phase shift of open/shorted-stub-loaded TL at f_0 is always unchanged and the same with θ_1. But the phase shifts at the operating frequencies except of f_0 are varied with θ_{open}, θ_{short}, Z_{open}, Z_{short}, and Z_1 even keeping the conditions of $\theta_{short} + \theta_{open} = 90^\circ$ and $Z_{open} = Z_{short}$. In other words, at the above condition, the slope of the phase-frequency relationship can be adjusted by the circuit parameters without affecting the phase shifts at the center frequency.

In the following, two examples are provided to explain the procedures for obtaining the circuit parameters of the C-PSs and F-PSs.

Firstly, the C-PS inserted before port 7 (denoted as C-PS3) is investigated. Figure 4 shows the phase variations of C-PS3 with different circuit parameters (θ_{open}, Z_{open}, and Z_1). It is noted that when changing one parameter, the others are at the optimized value. It is seen from Figure 4 that the slope of the phase is increased with the increasing of θ_{open} and Z_1 and the decreasing of Z_{open}. Besides, the slope of the phase is more affected by the θ_{open}. Based on

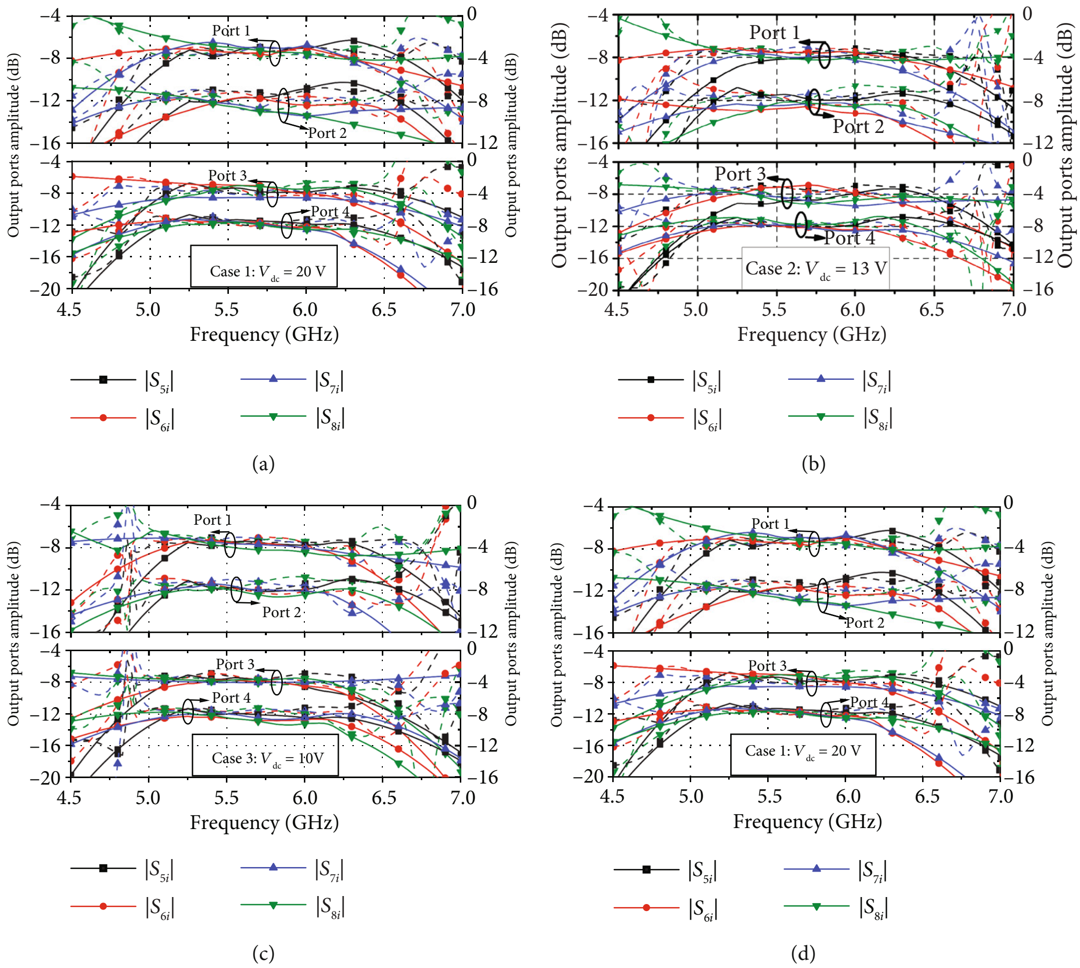

Figure 12: Simulated and measured output port amplitude (measured results: solid line with symbol, simulated results: dash line with symbol). (a) Case 1, (b) case 2, (c) case 3, and (d) case 4.

the adjusting rules in Figure 4, the phase slope at port 7 is changed to be similar with port 8 for obtaining flat output PD.

Figure 5 shows the PD between ports 7 and 8 without and with the C-PS3 when port 1 is excited. According to the dashed line, it can be seen that without the C-PS3, the slope of the PD is about 101.3°/GHz and the relative bandwidth for ±10° error is only 3.4%. To obtain a flat PD, the phase slope at port 7 is varied with the help of the inserted C-PS3. Here, the phase slope at port 8 is served as a reference. According to (15), the circuit parameters in C-PS3 are obtained as follows: $\theta_{open} = 62.3°$, $Z_{open} = 63.6\,\Omega$, and $Z_1 = 53.9\,\Omega$. Obviously, according to the solid line in Figure 5, after compensation using C-PS3, the PD between ports 7 and 8 is flatted and the relative bandwidth for ±10° error is increased to be more than 25%.

Secondly, the 180° F-PS in the PS with a phase shift of φ_4 is studied. Taking port 2 excitation as an example, two paths are involved in signal transmission to port 6. Here, the different phase slope of the two paths is related to the 360° line and the 180° F-PS. In general, all the paths for the same output port should keep the same phase slope for simplified analysis. Thus, the phase slope of the 180° F-PS in φ_4 should be equal with the 360° line. Equation (16) expresses the phase-frequency relationship of a 360° line. By equaling (15) with (16), the parameters in the 180° F-PS are obtained.

$$\theta(f) = 360 \circ \frac{f}{f_0}. \tag{16}$$

As an illustration, the variations of the phase slope in the 180° F-PS are plotted in Figure 6. In the figure, the phase-frequency curve for the 360° line is also given and is served as a reference in compensation. The slope of the phase for the 360° line is about 61.7°/GHz. Since from the varying rules in Figure 6 that the phase slope is more influenced by θ_{open}, the phase-frequency curve for the 180° F-PS versus different θ_{open} is investigated. Here, the values of Z_{open} and Z_1 are defined as 70 Ω and 60 Ω, respectively. With the decreasing of θ_{open}, the slope of the 180° F-PS is decreased. At $\theta_{open} = 45.6°$, the phase slope of the 180° F-PS is about 60.1°/GHz which is close to the phase slope of the 360° line.

In the same way, the circuit parameters in other C-PSs and the 90° F-PS can be achieved. Here, the C-PS inserted before port 6 is defined as C-PS2, and the ones before port

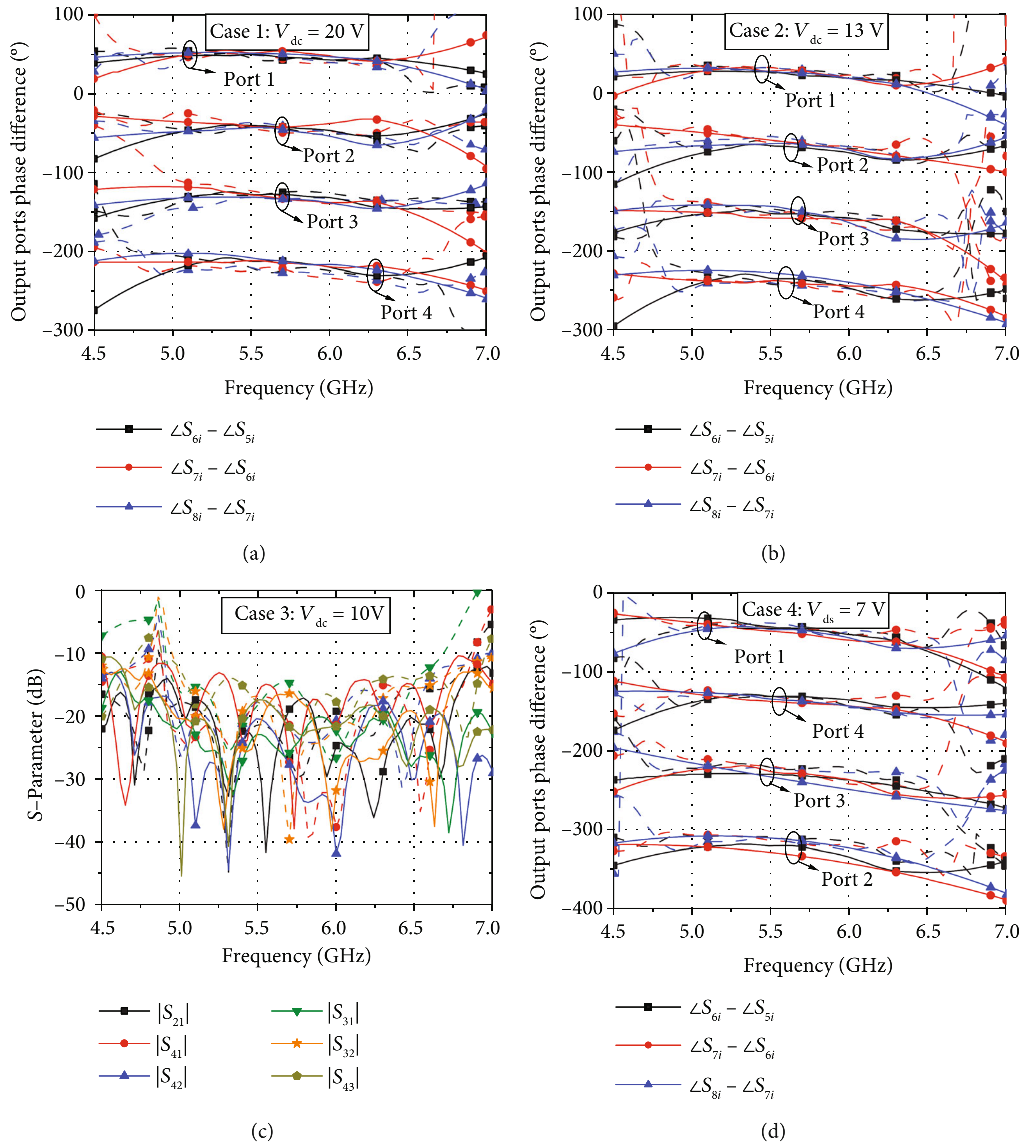

Figure 13: Simulated and measured output port phase differences (measured results: solid line with symbol, simulated results: dash line with symbol). (a) Case 1, (b) case 2, (c) case 3, and (d) case 4.

Table 5: Comparison between the proposed and reported phase tunable BFNs.

Ref.	Type	f_c (GHz)	FBW	RL & IO criterion	Maximum error AP	Maximum error PD	IL	PD range	T-PS range	T-PS location	No. of T-PS	No. of voltage	Continuously
[22]	4 × 4 Butler	2.4	8.3%	14 dB	—	±45°	1.7 dB	270°	2 bit PS	Cascade	3 (3 types)	3	No
[23]	3 × 3 Nolen	2.45	2.6%	—	2.5 dB	±10°	—	270°	90°	Cascade	2 (2 types)	4	Yes
[24]	4 × 4 Butler	5.8	15%	10 dB	±4 dB[a]	>40°[a]	4 dB	360°	90°/180°	Integrate	4 (2 types)	2	Yes
[25]	2 × 4 Butler	2.4	20%	10 dB	±1.4 dB	±18°	4 dB	360°	±180°	Integrate	6 (6 types)	6	Yes
This work	4 × 4 Nolen	5.8	24.5%	10 dB	±1.5 dB	±15°	2 dB	360°	90°	Integrate	6 (1 type)	1	Yes

[a]Estimate from the measured curves. FBW: fractional bandwidth.

5 are named as C-PS1. Table 2 illustrates the values of the different C-PSs and F-PSs in the proposed Nolen matrix. It is noted that since each of the extra C-PS before the output ports is used for compensating the phases introduced from a 180° TL and one T-PS, the circuit parameters of the designed C-PSs are identical. The circuit parameters of the designed C-PSs are identical. Figure 7 shows the PD comparisons before and after compensation at one tuning state. It is clear that all the relative bandwidths for ±10° PD error are improved from less than 4% to over 25%, which validate the effectiveness of the proposed compensation method.

4. Fabrication and Measurement

According to the aforementioned process, a wideband 4 × 4 Nolen matrix with continuously tuned differential phase and low in-band phase deviation error is constructed and fabricated on a Rogers 4350B substrate ($\varepsilon_r = 3.48$, tan $\delta = 0.0037$, $h = 0.762$ mm). Figures 8 and 9 show the layout and photograph of the designed prototype. Table 3 lists the dimensions of the designed Nolen matrix with the overall size of 174.1 mm × 100 mm. Since tight coupling (3 dB) is needed for realizing the T-PS, the structure in [32] is utilized in the layout, and the detailed structure of the T-PSs can be observed in Figure 8. The SMV2020-79F varactor [33] is adopted in this design, whose capacitance is varied from 3.2 pF to 0.5 pF by adjusting the bias voltage from 0 V to 20 V. According to the SPICE model illustrated in [33], the varactor can be modeled in the ADS software. Figure 8 gives the equivalent circuit of the varactor with the labeled parasitic parameters.

Since the six T-PSs in the Nolen matrix are the same, one voltage V_{dc} is enough in the control. Each of the bias circuits is composed of one resistor of 10 kΩ and a blocking capacitor of 1 μF. It is noted since the resistor is served as the same function with a blocking inductor and is less sensitive to the value error than the inductor, the resistor is applied in this implementation.

Table 4 shows the output ports PDs of the Nolen matrix at 5.8 GHz corresponding to different bias voltages. It is found that when V_{dc} changes from 20 V to 7 V, the output ports PDs for port 1 excitation range from 49° to -48°. When port 4 is excited, the output ports PDs are in the range of -42° to -134°. When the signals are input from ports 2 and 3 separately, the output ports PDs are within -134° to -232° and -226° to -319°. Thus, a full 360° continuously tuned differential phase is realized.

To illustrate more clearly, the performances of the designed prototype under voltage values of 20 V, 13 V, 10 V, and 7 V are plotted, as shown in Figures 10–13. The four conditions are named as cases 1, 2, 3, and 4, respectively.

As shown in Figure 10, for case 1, the frequency range for $|S_{11}| - |S_{44}| < -10$ dB is within 5 GHz-6.6 GHz, yielding a 10 dB impedance bandwidth of 20.6%. For case 2, all the measured RLs are less than -10 dB from 5 GHz to 6.5 GHz (20.6%). For cases 3 and 4, the 10 dB RL is 20.1% and 20.5%, respectively. And according to Figure 11, the isolations (IO) are both larger than 10 dB in the four cases from 5 GHz to 6.4 GHz.

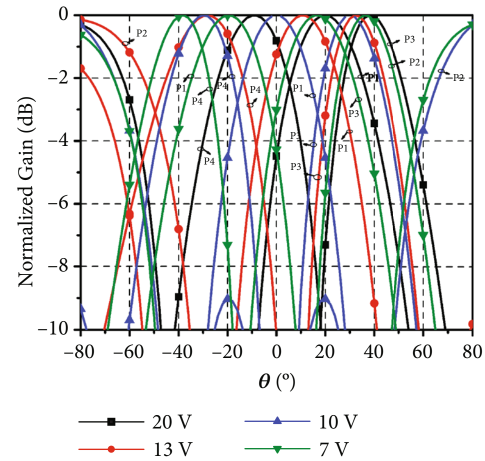

Figure 14: The calculated radiation pattern for different voltages.

Figure 12 shows the output port AP distributions of the 4 × 4 Nolen matrix, where the values of around -8 dB are obtained at the four cases. The extra insertion loss (IL) of nearly 2 dB is mainly due to the loss of the substrate, the insertion loss of the T-PS, and the influence of the DC power supply. At case 1, the bandwidths for output port AP within −8 dB ± 1 dB are 20.4%, 15.2%, 18.2%, and 22.4%, separately, when ports 1, 2, 3, and 4 are excited. When the voltage is changed to 13 V, the bandwidths are 21.7%, 16.9%, 20.3%, and 22.8%, respectively. For case 3, the −8 ± 1 dB bandwidths are 22.3%, 20.1%, 20.3%, and 21.8%, separately. Finally, the bandwidths are 20.6%, 17.4%, 16.3%, and 20.1% for case 4, respectively.

The output ports PDs of the designed Nolen matrix are shown in Figure 13. At case 1, the output port PD are 49°, -134° and -226°, and -42°, respectively, at the center frequency of 5.8 GHz when different input ports are excited. Under the criterion of 20° PD error, the bandwidths are 21.6%, 22.4%, 20.9%, and 21.8%, separately. When the voltage is changed to 13 V, the output port phase differences are 27°, -151°, -244°, and -68° at 5.8 GHz. And the corresponding bandwidths for PD error within 20° are 22.3%, 19.8%, 21.2%, and 20.9%. In case 3, the bandwidths for 0° ± 10°, −181° ± 10°, −261° ± 10°, and −89° ± 10° are 24.3%, 22.6%, 21.1%, and 18.9%, respectively. And the values are 20.1%, 21.4%, 18.3%, and 17.6% for case 4 at the PDs of −48° ± 10°, −232° ± 10°, −319° ± 10°, and −134° ± 10°.

Table 5 illustrates the performance comparisons between the proposed and representative designs. In [22, 23], reconfigurable PSs and tunable PSs are cascaded to the output ports of the network. However, the bandwidths are less than 10%, and the in-band PD error is large for the network in [22]. For the networks in [24, 25], the T-PSs are integrated in the network which indicates that tunable differential phase can be obtained without enlarging the circuit size. Although wide bandwidth of 15% and full PD range of 360° is achieved in [24], the in-band PD error is larger than 40°. Besides, the AP error and IL are large compared with others. Compared with the network in [25], the proposed

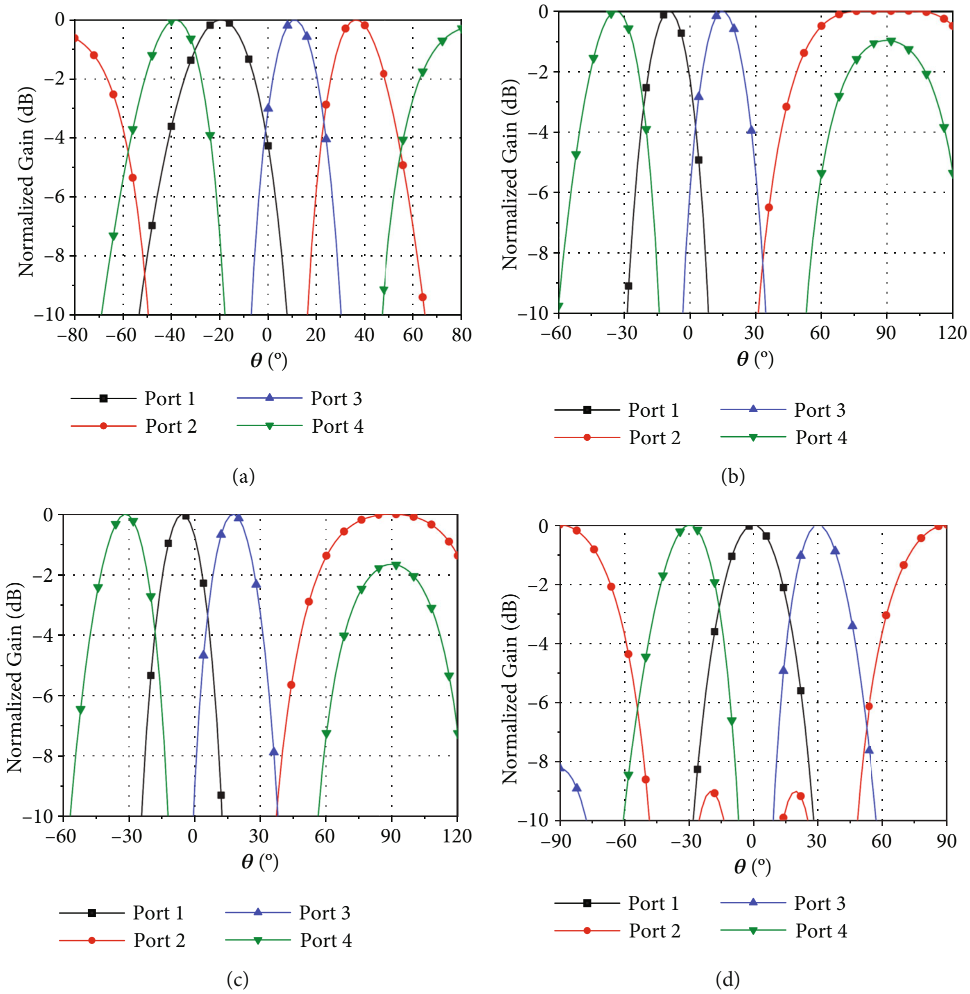

Figure 15: The calculated radiation patterns for detailed voltage range. (a) 7 V. (b) 8 V. (c) 9 V. (d) 10 V.

design exhibits wider bandwidth with low in-band PD error, lower loss, and smaller range of T-PS. Although the design requires six T-PSs, the phase shift range of the T-PS used is small, and all T-PSs are controlled simultaneously by only one DC power, so the phase control process of this design is greatly simplified compared to other structures.

5. Discussions

In this section, the radiation patterns of a 1×4 array under different voltages are investigated to further evaluate the performance of the proposed beamforming network.

Figure 14 shows the calculated array pattern when the voltages are 20 V, 13 V, 10 V, and 7 V for excitation at different ports, where the distance of the array element is 0.6λ. It can be seen that the scanning angle can cover the range of about ±45°, which shows that as long as the voltage step is small enough, any beam angle in the range of ±45° can be realized. It is noted that when the voltages are 10 V and 13 V for port 2 excitation, the phase differences are both large (-151° and -180°), results in that the beam pointing is out of the range of ±45°.

Moreover, to clearly understand the variations of the beam pointing for different input ports, the radiation patterns for a more detailed voltage range of 7 V-10 V are plotted, as shown in Figure 15. At the voltage of 7 V, the maximum radiation directions for ports 1 to 4 excitation are -18°, 36°, 10°, and -38°, respectively. At 8 V, the beam angles are changed to -10°, 76°, 14°, and -34°. Finally, at 9 V and 10 V, the angles are -6°, 84°, 18°, -32° and 0°, 90°, 28°, and -30°, respectively. It is clear that as the voltage increases, the beam angles corresponding to the four input ports are all shifted to the right side. And when the phase difference is large, the beam pointing changes more obviously. For example, when port 2 is excited, when the voltage rises from 7 V to 8 V, the beam pointing changes from 36° to 76°. In other cases, the beam pointing changes within 10° when the voltage is increased by 1 V.

6. Conclusion

A wideband continuous tunable phase progression beamforming network with one type of T-PS controlled by one voltage is demonstrated in the paper. By using the T-PS with a phase shift range of 90°, full 360° differential phase variation is achieved at the output ports. Besides, the in-band output port AP and PD errors are minimized based on the phase slope compensation technique. A 4×4 matrix prototype is fabricated and measured. Measurement results show that a wide bandwidth of 24.5% is achieved with 10 dB RL, 10 dB IO, ±1.5 dB AP imbalance, and 15° PD error. Moreover, under more strictly criterions of ±1 dB AP imbalance and 10° PD error, the bandwidth is larger than 15%, which indicates the applications in MIMO radar and 5G multibeam systems with a high figure of merit.

Data Availability

The data used to support the findings of this study are included within the article.

Conflicts of Interest

The authors declare that they have no conflicts of interest.

Acknowledgments

This work was supported in part by the National Natural Science Foundation of China under Grant 51809030, in part by the Liaoning Revitalization Talents Program under Grant XLYC2007067, in part by the Young Elite Scientists Sponsorship Program by CAST under Grant 2022QNRC001, and in part by the Fundamental Research Funds for the Central Universities under Grant 3132023246.

References

[1] J. Butler and R. Lowe, "Beamforming matrix simplifies design of electrically scanned antennas," *Electronic Design*, vol. 9, no. 4, pp. 170–173, 1961.

[2] J. Blass, "Multidirectional antenna - a new approach to stacked beams," in *1958 IRE International Convention Record*, pp. 48–50, New York, NY, USA, March 1966.

[3] J. Nolen, *Synthesis of Multiple Beam Networks for Arbitrary Illuminations*, Ph.D. dissertation, Dept. Radio Division, Bendix Corp., Baltimore, MD, USA, 1965.

[4] S.-K. Zhao, M. Lv, Z. Zhang, Q. Chen, and G. Fu, "Planar two-dimensional scanning multibeam array antenna based on a 3×3 Butler matrix network," *IEEE Antennas and Wireless Propagation Letters*, vol. 21, no. 6, pp. 1163–1167, 2022.

[5] Q. P. Chen, Z. Qamar, S. Y. Zheng, Y. Long, and D. Ho, "Design of a compact wideband Butler matrix using vertically installed planar structure," *IEEE Transactions on Components, Packaging and Manufacturing Technology*, vol. 8, no. 8, pp. 1420–1430, 2018.

[6] P. Li, H. Ren, and B. Arigong, "A symmetric beam-phased array fed by a Nolen matrix using 180° couplers," *IEEE Microwave and Wireless Components Letters*, vol. 30, no. 4, pp. 387–390, 2020.

[7] H. Ren, H. Zhang, Y. Jin, Y. Gu, and B. Arigong, "A novel 2-D 3×3 Nolen matrix for 2-D beamforming applications," *IEEE Transactions on Microwave Theory and Techniques*, vol. 67, no. 11, pp. 4622–4631, 2019.

[8] Z. Wang, C. Li, P. Han, H. Liu, and S. Fang, "A novel 3×3 Nolen matrix based on trans-directional coupled lines," in *2021 Photonics & Electromagnetics Research Symposium (PIERS)*, pp. 1573–1577, Hangzhou, China, November 2021.

[9] H. Ren, H. Zhang, and B. Arigong, "Ultra-compact 3×3 Nolen matrix beamforming network," *IET Microwaves, Antennas & Propagation*, vol. 14, no. 3, pp. 143–148, 2020.

[10] N. J. G. Fonseca, "Printed S-band 4×4 Nolen matrix for multiple beam antenna applications," *IEEE Transactions on Antennas and Propagation*, vol. 57, no. 6, pp. 1673–1678, 2009.

[11] H. Ren, H. Zhang, P. Li, Y. Gu, and B. Arigong, "A novel planar Nolen matrix phased array for MIMO applications," in *2019 IEEE International Symposium on Phased Array System & Technology (PAST)*, pp. 1–4, Waltham, MA, USA, October 2019.

[12] N. J. G. Fonseca and N. Ferrando, "Nolen matrix with tapered amplitude law for linear arrays with reduced side lobe level," in *Proceedings of the Fourth European Conference on Antennas and Propagation*, pp. 1–5, Barcelona, Spain, April 2010.

[13] G. Tian, J.-P. Yang, and W. Wu, "A novel compact Butler matrix without phase shifter," *IEEE Microwave and Wireless Components Letters*, vol. 24, no. 5, pp. 306–308, 2014.

[14] H. Ren, B. Arigong, M. Zhou, J. Ding, and H. Zhang, "A novel design of 4×4 Butler matrix with relatively flexible phase differences," *IEEE Antennas and Wireless Propagation Letters*, vol. 15, pp. 1277–1280, 2016.

[15] A. Karimbu Vallappil, M. K. A. Rahim, B. A. Khawaja, and M. N. Iqbal, "Compact metamaterial based 4×4 Butler matrix with improved bandwidth for 5G applications," *IEEE Access*, vol. 8, pp. 13573–13583, 2020.

[16] S. Gruszczynski and K. Wincza, "Broadband 4×4 Butler matrices as a connection of symmetrical multisection coupled-line 3-dB directional couplers and phase correction networks," *IEEE Transactions on Microwave Theory and Techniques*, vol. 57, no. 1, pp. 1–9, 2009.

[17] K.-R. Xiang, F.-C. Chen, Q.-X. Chu, and M. J. Lancaster, "A broadband 3×4 Butler matrix and its application in multibeam antenna arrays," *IEEE Transactions on Antennas and Propagation*, vol. 67, no. 12, pp. 7622–7627, 2019.

[18] Y. Yang, Y. F. Pan, S. Y. Zheng, W. Hong, and W. S. Chan, "Analytical design method and implementation of broadband 4×4 Nolen matrix," *IEEE Transactions on Microwave Theory and Techniques*, vol. 70, no. 1, pp. 343–355, 2022.

[19] J. M. Wen, C. K. Wang, W. Hong, Y. M. Pan, and S. Y. Zheng, "A wideband switched-beam antenna array fed by compact single-layer Butler matrix," *IEEE Transactions on Antennas and Propagation*, vol. 69, no. 8, pp. 5130–5135, 2021.

[20] H. Zhu, T. Zhang, and Y. J. Guo, "Wideband hybrid couplers with unequal power division/arbitrary output phases and applications to miniaturized Nolen matrices," *IEEE Transactions on Microwave Theory and Techniques*, vol. 70, no. 6, pp. 3040–3053, 2022.

[21] L. Ma, Y. Wu, and W. Wang, "Design of wideband Butler matrix with equal/unequal phase differences for flexible beam-controllability," *IEEE Transactions on Circuits and Systems II: Express Briefs*, vol. 68, no. 12, pp. 3537–3541, 2021.

[22] H. N. Chu and T. G. Ma, "An extended 4×4 Butler matrix with enhanced beam controllability and widened spatial coverage," *IEEE Transactions on Microwave Theory and Techniques*, vol. 66, no. 3, pp. 1301–1311, 2018.

[23] J.-Z. Cao and F.-C. Chen, "A tunable Nolen matrix based on reconfigurable phase shifters," in *2021 13th International*

Symposium on Antennas, Propagation and EM Theory (ISAPE), pp. 1–3, Zhuhai, China, December 2021.

[24] H. Ren, P. Li, Y. Gu, and B. Arigong, "Phase shifter-relaxed and control-relaxed continuous steering multiple beamforming 4×4 Butler matrix phased array," *IEEE Transactions on Circuits and Systems I: Regular Papers*, vol. 67, no. 12, pp. 5031–5039, 2020.

[25] H. N. Chu, T. H. Hoang, K.-J. Ji, and T.-G. Ma, "A phase distribution network using 2 × 4 Butler matrix for linear/planar beam-scanning arrays," *IEEE Access*, vol. 9, pp. 133438–133448, 2021.

[26] H. Zhu and A. M. Abbosh, "A compact tunable directional coupler with continuously tuned differential phase," *IEEE Microwave and Wireless Components Letters*, vol. 28, no. 1, pp. 19–21, 2018.

[27] B. W. Xu, S. Y. Zheng, W. M. Wang, Y. L. Wu, and Y. A. Liu, "A coupled line-based coupler with simultaneously tunable phase and frequency," *IEEE Transactions on Circuits and Systems I: Regular Papers*, vol. 66, no. 12, pp. 4637–4647, 2019.

[28] Y. F. Pan, S. Y. Zheng, W. S. Chan, and H. W. Liu, "Compact phase-reconfigurable couplers with wide tuning range," *IEEE Transactions on Microwave Theory and Techniques*, vol. 68, no. 2, pp. 681–692, 2020.

[29] D. Yu, H. Liu, S. Li, Z. Wang, and S. Fang, "Control-relaxed wideband 2×4 Nolen matrix with 360° continuously tuned differential phase," *IEEE Transactions on Circuits and Systems II: Express Briefs*, 2023.

[30] C. A. Guo and Y. J. Guo, "A general approach for synthesizing multibeam antenna arrays employing generalized joined coupler matrix," *IEEE Transactions on Antennas and Propagation*, vol. 70, no. 9, pp. 7556–7564, 2022.

[31] M. Muraguchi, T. Yukitake, and Y. Naito, "Optimum design of 3-dB branch-line couplers using microstrip lines," *IEEE Transactions on Microwave Theory and Techniques*, vol. 31, no. 8, pp. 674–678, 1983.

[32] C. -H. Liang, W. -S. Chang, and C. -Y. Chang, "Enhanced coupling structures for tight couplers and wideband filters," *IEEE Transactions on Microwave Theory and Techniques*, vol. 59, no. 3, pp. 574–583, 2011.

[33] *Data Sheet-SMV2019 to SMV2023 Series: Hyperabrupt Junction Tuning Varactors*, Skyworks Solutions Inc., Woburn, MA, USA, 2020.